Dyes and Pigments 243 (2025) 113050

Contents lists available at ScienceDirect

Dyes and Pigments

journal homepage: www.elsevier.com/locate/dyepig

Ionic liquid crystals containing pyridinium and pyrazolium units: mesomorphism and acidochromic behaviors

Rosario Criado [a], Frederico Duarte [b], Irene Caro-Campos [c], Mercedes Cano [a], Santiago Herrero [a,d], Carlos Lodeiro [b,e,*], Cristián Cuerva [a,**]

[a] MatMoPol Research Group, Inorganic Chemistry Department, Faculty of Chemical Sciences, Complutense University of Madrid, Ciudad Universitaria, E-28040, Madrid, Spain
[b] BIOSCOPE Research Group, LAQV-REQUIMTE, Department of Chemistry, NOVA School of Science and Technology, FCT NOVA, NOVA University Lisbon, Caparica, 2829-516, Portugal
[c] Institute of Chemical Research (IIQ), Department of Inorganic Chemistry and Center for Innovation in Advanced Chemistry (ORFEO-CINQA), University of Sevilla and the Spanish National Research Council (CSIC), 41092, Sevilla, Spain
[d] Knowledge Technology Institute, Complutense University of Madrid, Campus de Somosaguas, 28223 Pozuelo de Alarcón, Madrid, Spain
[e] PROTEOMASS Scientific Society, Costa da Caparica, 2825-466, Portugal

ARTICLE INFO

Keywords:
Ionic salts
Liquid crystals
Smectic mesophase
Luminescence
Polymer sensor

ABSTRACT

Ionic liquid crystals are soft materials whose mesomorphic behavior can be strategically modulated as a function of their components, considering both the design of the organic cation and the nature of the inorganic anion. A new pyridylpyrazole derivative has been synthesized and used as a precursor for obtaining ionic salts that contain the corresponding dicationic fragment and different counterions. Most salts behave as liquid crystal materials exhibiting smectic A mesophases at temperatures ranging between 99 and 295 °C, as well as luminescence behavior in solution and/or the solid state. Interestingly, the related chloride salt emits blue light in the solid state under excitation at 261 nm, in contrast to the absence of the emission of the initial pyridylpyrazole derivative. This turn-on fluorescence response has been exploited to fabricate polymer supports that show a bright blue emission under exposure to hydrochloric acid.

1. Introduction

The functionalization of β-diketones or pyrazoles with pyridine moieties is a common strategy to prepare metallomesogens as they present several donor atoms in their structures that can be used for obtaining coordination compounds with liquid crystal properties [1]. For example, when designing β-diketones for use as ligands, the location of the pyridyl nitrogen atom in the three or four position favors the coordination of the diketone in a monodentate fashion via the pyridyl nitrogen atom [2]. Whereas, when the nitrogen atom of the pyridine moiety is located at the two position, pyrazoles can be easily coordinated to a metal center via the pyridyl and pyrazole nitrogen atoms in a chelate fashion [3–6].

Protonation of the pyridine gives also access to the fabrication of ionic liquid crystals, opening a wide range of possibilities as a function of the nature of both the cation and anion used [7–12]. Simple N-methylated pyridinium cations bearing aliphatic long chains were probably one of the first ionic salts exhibiting liquid crystalline phases [13]. These salts are capable of self-assembling into micelles or vesicles in solution due to their amphiphilic character but also form smectic mesophases in the solid state by the effect of temperature. Since then, a great variety of structural designs derived from the functionalization of the pyridinium cation have been reported as building blocks of ionic liquid crystals, including polycationic pyridinium salts [7].

In the past decade, we have explored different synthetic routes to prepare β-diketone pyridinium ionic salts with liquid crystal behavior [14]. Learning to control the organization that these salts adopt in the mesophase has allowed us to design materials with additional

* Corresponding author. BIOSCOPE Research Group, LAQV-REQUIMTE, Department of Chemistry, NOVA School of Science and Technology, FCT NOVA, NOVA University Lisbon, Caparica, 2829-516, Portugal.
** Corresponding author. MatMoPol Research Group, Inorganic Chemistry Department, Faculty of Chemical Sciences, Complutense University of Madrid, Ciudad Universitaria, E-28040, Madrid, Spain.
E-mail addresses: cle@fct.unl.pt (C. Lodeiro), c.cuerva@ucm.es (C. Cuerva).

https://doi.org/10.1016/j.dyepig.2025.113050
Received 16 May 2025; Received in revised form 16 July 2025; Accepted 17 July 2025
Available online 19 July 2025

functionalities such as luminescence or dielectric conductivity in the mesophase [2,14]. The protonation of the pyridine moiety usually causes drastic changes in the HOMO and LUMO frontier orbitals, allowing new charge-transfers that originate an enhancement of the emission properties in the dye [15]. On the other hand, the presence of ions that are allowed to freely move throughout the nanochannels of the mesophase makes these ionic salts promising materials as ionic conductors [16–18].

Less attention has been paid to the design of pyrazolium-based ionic salts. Herein, a new pyrazole (**1**) functionalized with a tetradecyloxyphenyl group and a pyridine moiety with the nitrogen atom at the three position has been synthesized. As is well-known, the pyrazole moiety contains a pyridinic nitrogen atom that is susceptible to being protonated. Thus, this species has been used to obtain the cation $[H_2pz^{R(14)Hpy}]^{2+}$, which in turn has allowed the obtention of the ionic salts **2**–**7**, isolated with counterions of different nature such as BF_4^-, SbF_6^- or $[PtCl_4]^{2-}$. Table 1 collects the numbering used to identify the new compounds.

2. Experimental Section

2.1. Starting materials

Solvents were purchased from Merck and used without further purification. The starting 1-(3-pyridyl)-3-(4-tetradecanoyloxyphenyl)propane-1,3-dione used for the preparation of the new pyrazole $Hpz^{R(14)py}$ was synthesized as previously reported [2].

2.2. Instrumentation

2.2.1. Structural characterization

FTIR spectra were recorded in the solid state on a PerkinElmer Spectrum 100 FTIR spectrophotometer with a universal ATR accessory in the region of 4000–650 cm^{-1}. ^1H NMR and 2D COSY spectra were performed on a Bruker DPX-300 spectrophotometer (NMR Service at Complutense University of Madrid) from solutions in $CDCl_3$ or DMSO-d_6 at room temperature. Chemical shifts δ are listed relative to $SiMe_4$ (TMS) by using the signal of the deuterated solvent as a reference and coupling constants J are given in Hertz. Multiplicities are indicated as follows: s (singlet), d (doublet), t (triplet), qt (quintet), dd (doublet of doublets), ddd (doublet of doublets of doublets), m (multiplet), br (broad signal). The ^1H shifts are accurate to ±0.01 ppm and coupling constants to ±0.3 Hz.

2.2.2. Mesomorphic studies

Polarized light optical microscopy (POM) observations were carried out by using an Olympus BX50 microscope equipped with a Linkam THMS 600 heating stage. The transition temperatures and their associated enthalpy data were determined with a PerkinElmer Pyris 1 differential scanning calorimeter. Samples were hermetically sealed in aluminum pans and measurements were carried out with heating and cooling rates of 10 K min^{-1}. Temperature-dependent powder X-ray diffraction (XRD) studies were carried out on a Panalytical X'Pert PRO MPD diffractometer with Cu-Kα (1.54 Å) radiation in a θ–θ configuration equipped with an Anton Paar HTK1200 heating stage (X-Ray Diffraction Service at the Complutense University of Madrid).

Table 1
Compounds described in this work, including the numbering used to identify them.

Numbering	Compound
1	$Hpz^{R(14)py}$
2	$(H_2pz^{R(14)Hpy})Cl_2$
3	$(H_2pz^{R(14)Hpy})(BF_4)_2$
4	$(H_2pz^{R(14)Hpy})Cl(PF_6)$
5	$(H_2pz^{R(14)Hpy})(OH)(SbF_6)$
6	$(H_2pz^{R(14)Hpy})[PtCl_4]$
7	$(H_2pz^{R(14)Hpy})[PdCl_4]$

2.2.3. Spectrophotometric and spectrofluorimetric measurements

All compounds were photophysically characterized by using a JASCO V-650 spectrophotometer and a Horiba-Jobin-Yvon Fluoromax-4 spectrofluorometer to obtain the UV–Vis absorption spectra, as well as the emission, excitation, and solid-state emission ones. For this latter, a coupled fiber-optics device was connected to the spectrofluorometer, and the solid sample was excited at the appropriate wavelength. All measurements were performed in the PROTEOMASS-BIOSCOPE facilities at LAQV-REQUIMTE, NOVA University Lisbon. In order to obtain the referred spectra in solution, a proper amount of the different compounds was dissolved in a 10 mL volumetric flask in THF so that a stock solution (*ca.* 10^{-3} M) could be obtained. The work solutions were prepared by proper dilution of the stock solutions to 10^{-6} M, and the measurements were collected by choosing the appropriate wavelength at 298 K.

2.2.4. Theoretical calculations

These calculations were performed using the Gaussian 16(C01) package (DFT) [19], employing Coulomb-Attenuating Method B3LYP (CAM-B3LYP) [20]. This functional better reproduces the charge transfer (CT) states [21]. The H, C, O and N atoms were represented with the 6-31+G(2d,p) basis set [22]. The structures were optimized without any geometric constraints using the SMD continuum solvent model (THF) and in the gas phase [23]. To reduce calculation cost, the terminal alkyl chains were replaced by methyl group. In order to calculate the molecular electrostatic (MEP) surface maps, natural bond orbital (NBO) atomic charges and frontier orbitals, analyses were performed at the same level of theory from the structures that had previously been optimized. The visualization of molecular structures, orbitals and MEP surfaces was carried out using Chemcraft and VMD software [24,25]. TD-DFT studies were carried out using the same level of theory as the ground state (GS) optimizations to obtain the excited-state (ES) structures, both in the gas phase and in THF solvent [26].

2.2.5. Synthetic procedures

*2.2.5.1. Synthesis of the pyrazole $Hpz^{R(14)py}$ (**1**).* To a solution of the starting pyridine-functionalized diketone (1 g, 2.36 mmol) in ethanol (40 mL, 96 % v/v), another ethanol solution (40 mL) of hydrazine monohydrate (0.12 g, 2.36 mmol) was slowly added. The mixture reaction was refluxed for 24 h and then, it was cooled to room temperature to yield a beige precipitate, which is filtered off and dried under vacuum.

Beige solid (12 %). FTIR data (cm^{-1}): 3197–3008 ν(C–H)$_{arom.}$, 2955–2851 ν(C–H)$_{aliph.}$, 1513–1438 ν(C═C) + ν(C═N), 772 δ(C–H)$_{py}$. ^1H NMR data (ppm), δ_H (300.16 MHz; $CDCl_3$; TMS), 0.88 (3H, t, ^3J 6.9, CH_3), 1.26–1.47 (22H, m, CH_2), 1.80 (2H, m, CH_2), 3.99 (2H, t, ^3J 6.6, OCH_2), 6.79 (1H, s, H_4), 6.97 (2H, d, ^3J 8.7, H_m), 7.37 (1H, dd, ^3J 7.9, $H_{5'}$), 7.57(2H, d, ^3J 8.7, H_o), 8.12 (1H, dt, ^3J 7.9, $H_{4'}$), 8.57 (1H, d, ^3J 4.8, $H_{6'}$), 9.07 (1H, s, $H_{2'}$). δ_H (300.16 MHz; DMSO-d_6; TMS), 0.84 (3H, t, ^3J 6.8, CH_3), 1.22–1.41 (22H, m, CH_2), 1.71 (2H, m, CH_2), 3.99 (2H, t, ^3J 6.5, OCH_2), 7.02 (2H, d, ^3J 8.2, H_m), 7.17 (1H, s, H_4), 7.44 (1H, m, $H_{5'}$), 7.71 (2H, d, ^3J 8.5, H_o), 8.18 (1H, d, ^3J 7.9, $H_{4'}$), 8.51 (1H, m, $H_{6'}$), 9.05 (1H, s, $H_{2'}$), 13.34 (1H, s, NH). Found: C, 77.17 %; H, 9.06 %; N 8,93 %, molecular formula $C_{28}H_{39}N_3O$ requires: C, 77.11 %; H, 8.87 %; N, 8.97 %.

*2.2.5.2. Synthesis of the ionic salt $(H_2pz^{R(14)Hpy})Cl_2$ (**2**).* To a solution of the pyrazole $Hpz^{R(14)py}$ (0.27 g, 0.65 mmol) in tetrahydrofuran (50 mL), a diluted aqueous solution of HCl (6 M) was slowly added up to achieve a pH value of 2. The mixture was stirred at room temperature for 3 h. The obtained precipitate was filtered off and dried under vacuum.

Beige solid (83 %). FTIR data (cm^{-1}): 3482 ν(O–H), 3086 ν(C–H)$_{arom}$,

2915–2847 ν(C–H)$_{aliph.}$, 2564 ν(N–H)$^{+}_{NH}$, 1635–1491 ν(C=N) + ν(C=C), 820 δ(C–H)$_{py}$. ^{1}H NMR data (ppm), δ_H (300.16 MHz; DMSO-d_6; TMS), 0.84 (3H, t, ^{3}J 6.6, CH_3), 1.23–1.41 (22H, m, CH_2), 1.72 (2H, q, ^{3}J 6.3, CH_2), 4.01 (2H, t, ^{3}J 6.5, OCH_2), 7.05 (2H, d, ^{3}J 8.8, ^{4}J 3.1 H_m), 7.40 (1H, s, H_4), 7.73 (2H, d, ^{3}J 8.8, ^{4}J 2.97, H_o), 8.05 (1H, dd, ^{3}J 8.2, ^{4}J 5.6, H_5'), 8.82 (1H, d, ^{3}J 8.5, ^{4}J 1.6, H_6'), 8.88 (1H, dt, ^{3}J 5.6, ^{4}J 3.5, $H_{4'}$), 9.28 (1H, d, ^{4}J 2.0, $H_{2'}$). Found: C, 63.62 %; H, 8.02 %; N, 8.01 %, molecular formula $C_{28}H_{41}N_3OCl_2{\cdot}H_2O$ requires: C, 64.11 %; H, 8.26 %; N, 8.01 %.

*2.2.5.3. Synthesis of the ionic salt ($H_2pz^{R(14)Hpy}$)$(BF_4)_2$ (**3**).* A solution of the chloride salt ($H_2pz^{R(14)Hpy}$)Cl_2 (0.03 g, 0.06 mmol) in methanol (10 mL) was added over another solution of $AgBF_4$ (0.023 g, 0.12 mmol) in acetonitrile (10 mL). The reaction was stirred for 24 h at room temperature in absence of light. Then, the mixture was filtered over Celite®, and the resulting solution was concentrated up to a final volume of *ca.* 15 mL. The precipitate obtained after maintaining the suspension for 12 h at 4 °C was washed with chloroform, filtered off, and dried under vacuum.

Beige solid (15 %). FTIR data (cm^{-1}): 3161–3128 ν(C–H)$_{arom.}$, 2920–2851 ν(C–H)$_{aliph.}$, 2641 ν(N–H)$^{+}_{NH}$, 1615–1470 ν(C=N) + ν(C=C), 1058 ν(B–F), 784 δ(C–H)$_{py}$. ^{1}H NMR data (ppm), δ_H (300.16 MHz; DMSO-d_6; TMS), 0.84 (3H, t, ^{3}J 6.37, CH_3), 1.42–1.23 (22H, m, CH_2), 1.72 (2H, m, CH_2), 4.01 (2H, t, ^{3}J 6.4, OCH_2), 7.03 (2H, d, ^{3}J 8.5, H_m), 7.29 (1H, s, H_4), 7.73 (2H, d, ^{3}J 8.5, H_o), 7.79 (1H, dd, ^{3}J 5.19, $H_{5'}$), 8.56 (1H, d, ^{3}J 8.1, $H_{4'}$), 8.68 (1H, d, ^{3}J 5.1, $H_{6'}$), 9.18 (1H, s, $H_{2'}$). Found: C, 53.57 %; H, 6.56 %; N, 6.32 %, molecular formula $C_{28}H_{41}N_3OB_2F_8{\cdot}0.2CHCl_3$ requires: C, 53.50 %; H, 6.64 %; N, 6.56 %.

*2.2.5.4. Synthesis of the ionic salt ($H_2pz^{R(14)Hpy}$)$Cl(PF_6)$ (**4**).* A similar procedure than that carried out for **3** was used for the preparation of the compound ($H_2pz^{R(14)Hpy}$)$Cl(PF_6)$ (**4**), but using **2** (0.064 g, 0.126 mmol) and $AgPF_6$ (0.064 g, 0.25 mmol) instead of $AgBF_4$.

Beige solid (11 %). FTIR data (cm^{-1}): 3135–3014 ν(C–H)$_{arom.}$, 2923–2853 ν(C–H)$_{aliph.}$, 2626 ν(N–H)$^{+}_{NH}$, 1615–1554 ν(C=N)+ ν(C=C), 828 ν(P–F), 795 δ(C–H)$_{py}$. ^{1}H NMR data (ppm), δ_H (300.16 MHz; DMSO-d_6; TMS), 0.84 (3H, t, ^{3}J 6.4, CH_3), 1.23–1.41 (22H, m, CH_2), 1.72 (2H, m, CH_2), 4.00 (2H, t, ^{3}J 6.4, OCH_2), 7.02 (2H, d, ^{3}J 8.4, H_m), 7.18 (1H, s, H_4), 7.46 (1H, m, $H_{5'}$), 7.73 (2H, d, ^{3}J 8.3, H_o), 8.18 (1H, d, ^{3}J 8.1, $H_{4'}$), 8.52 (1H, d, ^{3}J 4.7, $H_{6'}$), 9.04 (1H, s, $H_{2'}$), 13.34 (1H, s, NH). Found: C, 55.05 %; H, 6.67 %; N, 6.34 %, molecular formula $C_{28}H_{41}N_3OClPF_6$ requires: C, 54.59 %; H, 6.82 %; N, 6.71 %.

*2.2.5.5. Synthesis of the ionic salt ($H_2pz^{R(14)Hpy}$)$(OH)(SbF_6)$ (**5**).* A similar procedure than that carried out for **3** was also used for the preparation of the compound ($H_2pz^{R(14)Hpy}$)$(OH)(SbF_6)$ (**5**), but using **2** (0.020 g, 0.04 mmol) and $AgSbF_6$ (0.028 g, 0.08 mmol) instead of $AgBF_4$.

Beige solid (18 %). FTIR data (cm^{-1}): 3396 ν(O–H), 3115–3014 ν(C–H)$_{arom.}$, 2923–2853 ν(C–H)$_{aliph.}$, 2626 ν(N–H)$^{+}_{NH}$, 1615–1554 ν(C=N) + ν(C=C), 795 δ(C–H)$_{py}$, 651 ν(Sb–F). ^{1}H NMR data (ppm), δ_H (300.16 MHz; DMSO-d_6; TMS), 0.84 (3H, t, ^{3}J 6.9, CH_3), 1.23–1.41 (22H, m, CH_2), 1.72 (2H, qt, ^{3}J 6.45, CH_2), 4.00 (2H, t, ^{3}J 6.45, OCH_2), 7.05 (2H, d, ^{3}J 8.8, ^{4}J 2.97 H_m), 7.32 (1H, s, H_4), 7.72 (2H, dt, ^{3}J 8.8, ^{4}J 3.03 H_o), 7.92 (1H, d, ^{3}J 6.8, $H_{5'}$), 8.73 (1H, m, $H_{4'}$), 8.73 (1H, m, $H_{6'}$), 9.21 (1H, s $H_{2'}$). Found: C, 48.65 %; H, 5.93 %; N, 6.07 %, molecular formula $C_{28}H_{42}O_2N_3SbF_6$ requires: C, 48.85 %; H, 6.15 %; N, 6.10 %.

*2.2.5.6. Synthesis of the ionic salt ($H_2pz^{R(14)Hpy}$)[$PtCl_4$] (**6**).* To a solution of ($H_2pz^{R(14)Hpy}$)Cl_2 (0.084 g, 0.16 mmol) in methanol (30 mL) is added another solution of $K_2[PtCl_4]$ (0.068 g, 0.16 mmol) in water (10 mL). After 1 h of stirring at room temperature, a precipitate is formed, which is filtered off and vacuum dried to yield the desired solid.

Beige solid (18 %). FTIR data (cm^{-1}): 3500–3481 ν(O–H), 3221–3059 ν(C–H)$_{arom.}$, 2922–2850 ν(C–H)$_{aliph.}$, 2644 ν(N–H)$^{+}_{NH}$, 1614–1467 ν(C=N) + ν(C=C), 789 δ(C–H)$_{py}$. ^{1}H NMR data (ppm), δ_H (300.16 MHz; DMSO-d_6; TMS), 0.84 (3H, t, ^{3}J 6.9, CH_3), 1.23–1.41 (22H, m, CH_2), 1.72 (2H, m, 2H), 4.01 (2H, t, ^{3}J 6.42, OCH_2), 7.04 (2H, d, ^{3}J 8.4, H_m), 7.30 (1H, s, H_4), 7.73 (2H, d, ^{3}J 8.1, H_o), 7.84 (1H, d, ^{3}J 7.1, $H_{5'}$), 8.60 (1H, d, ^{3}J 8.10, $H_{4'}$), 8.69 (1H, d, ^{3}J 5.2, $H_{6'}$), 9.19 (1H, s, $H_{2'}$). Found: C, 40.27 %; H, 4.88 %; N, 5.47 %, molecular formula $C_{28}H_{41}ON_3PtCl_4{\cdot}3H_2O$ requires: C, 40.68 %; H, 5.08 %; N, 5.73 %.

*2.2.5.7. Synthesis of the ionic salt ($H_2pz^{R(14)Hpy}$)[$PdCl_4$] (**7**).* A similar procedure than that carried out for **6** was used for the preparation of the compound ($H_2pz^{R(14)Hpy}$)[$PdCl_4$] (**7**), but using **2** (0.012 g, 0.020 mmol) and $K_2[PdCl_4]$ (0.008 g, 0.023 mmol) instead of $K_2[PtCl_4]$.

Beige solid (26 %). FTIR data (cm^{-1}): 3126 ν(C–H)$_{arom}$, 2922–2852 ν(C–H)$_{aliph.}$, 2625 ν(N–H)$^{+}_{NH}$, 1612–1461 ν(C=N) + ν(C=C), 794 δ(C–H)$_{py}$. Found: C, 49.78 %; H, 6.43 %; N, 5.85 %, molecular formula $C_{28}H_{41}N_3OPdCl_4$ requires: C, 49.18 %; H, 6.14 %; N, 6.04 %.

2.2.6. Preparation of PMMA doped thin films

The poly(methylmethacrylate) PMMA (Sigma-Aldrich, MW ~350,000, Tg 105 °C) polymer thin films were produced onto PFA supports with a diameter of 5 cm by dissolving 100 mg of the polymer matrix alongside 1 mg of $Hpz^{R(14)py}$ in 10 mL of $CHCl_3$, followed by slow evaporation of the solvent.

3. Results and discussion

3.1. Synthesis and structural characterization

The new pyrazole $Hpz^{R(14)py}$ (**1**) has been synthesized via a condensation reaction between the previously reported β-diketone and hydrazine monohydrate. As shown in Scheme 1, the reaction of **1** with $HCl_{(aq)}$ allowed obtaining the dichloride salt ($H_2pz^{R(14)Hpy}$)Cl_2 (**2**), which was in turn used as a precursor for the preparation of the ionic salts **3**–**7** via ionic interchange of the chloride anions.

The structural characterization of the compounds was carried out by FTIR and ^{1}H NMR spectroscopies. The proposed formulations were also confirmed by elemental analysis (see the Experimental Section).

The solid-state FTIR spectra of the pyrazole **1** and the ionic salts **2**–**7** show the expected bands for the pyrazole, pyridine, and alkyloxyphenyl moieties (Figs. S1–S7). It is interesting to highlight that the ν(C=N) and ν(C=C) bands, which appear at *ca.* 1510 cm^{-1} for **1**, are slightly shifted towards higher frequencies in the ionic salts. This feature suggests an increase of the strength of these bonds when the pyrazole and pyridyl nitrogen atoms are protonated. Likewise, the existence of the different counterions in **3**–**5** is also confirmed by the presence of the ν(B–F), ν(P–F), ν(F–P–F) and ν(Sb–F) bands at around 1018, 828, 559, and 652 cm^{-1}, respectively. On the other hand, note that a broad band centered between 2644 and 2564 cm^{-1} is observed for all ionic salts, which is assigned to the ν(N–H)$^{+}_{NH}$ band, in agreement with the protonation of the pyridyl and pyrazole nitrogen atoms [27]. In addition, note for compound **5**, a broad band at 3396 cm^{-1} is observed in agreement with the presence of the OH^- counterion. Results suggest that both in the PF_6^- and SbF_6^- salts, these bigger counterions were only able to replace one of the two chloride anions from the starting dichloride compound ($H_2pz^{R(14)Hpy}$)Cl_2.

The ^{1}H NMR spectra of the compounds were recorded in deuterated DMSO-d_6 solutions, and additionally pyrazole **1** was also characterized in deuterated $CDCl_3$ solution. Unfortunately, compound **7** is not soluble in common deuterated solvents and its NMR spectrum could not be obtained. In all spectra, three sets of signals associated with the protons of the pyridyl, alkyloxyphenyl and pyrazole moieties are observed. It is interesting to note that all the pyridyl proton signals appear downfield shifted with respect to those of the corresponding proton ones found for the neutral pyrazole, except for **4**, in which they appear almost unchanged (Figs. S8–S14). The NH signal of the pyrazole group was only

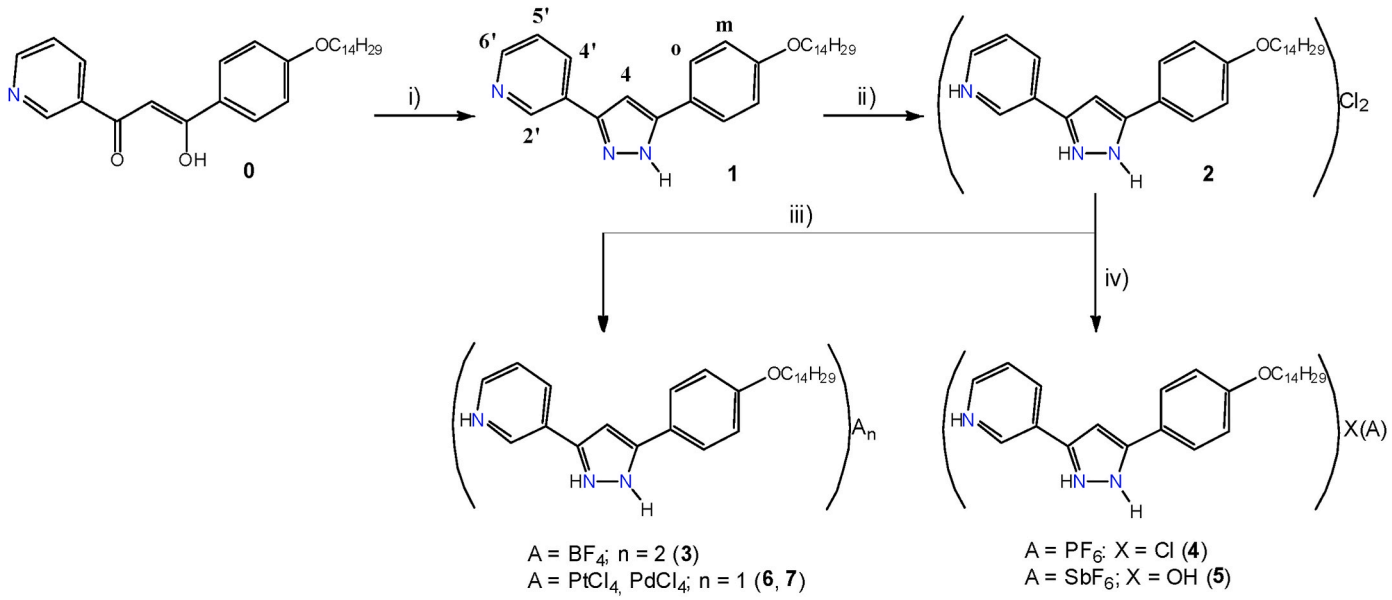

Scheme 1. Synthetic route for **1** and the ionic salts **2**–**7**. Reagent and conditions: i) $N_2H_4{\cdot}H_2O$, (EtOH, 24 h reflux); ii) HCl, THF, 3 h at RT; iii) $AgBF_4$ (MeOH: acetonitrile (1:1), 24 h at RT) or $K_2[PdCl_4]$ (MeOH:water (3:1), 1 h at RT) or $K_2[PtCl_4]$ (MeOH:water (3:1), 1 h at RT). iv) $AgPF_6$ or $AgSbF_6$ (MeOH:acetonitrile (1:1), 24 h at RT). Numbering used in the NMR assignation is also shown in the structural formula of **1**.

detected at 13.34 ppm for **1** and **4** in DMSO-d_6 solution. No signals associated with the pyrazole NH moiety are registered in the spectra of the remaining salts, which could be due to the establishment of intermolecular hydrogen bonds [28].

3.2. Mesomorphism

The liquid crystal properties and the phase behavior of the new compounds **1**–**7** were elucidated by microscopic observation of the samples under polarized light. The neutral pyrazole **1** directly melts to the isotropic liquid at 153 °C, and no intermediate phases between the solid and liquid states were detected. By contrast, the ionic salts (except **7**) form liquid-crystalline mesophases at temperatures that appear to depend on the nature of the counterion. As shown in Fig. 1a and S15, oily streak and fan-shaped textures of a SmA mesophase can be seen growing from the solid or the liquid phase upon heating or cooling cycles, respectively [29,30]. Differential scanning calorimetry (DSC) experiments were conducted to study the phase behavior of the ionic salts in terms of establishing the temperatures at which the phase transitions occur and their corresponding enthalpy values. Results are collected in Table 2. In all cases, the endothermic peak attributed to the solid – mesophase phase transition was clearly detected in the first heating

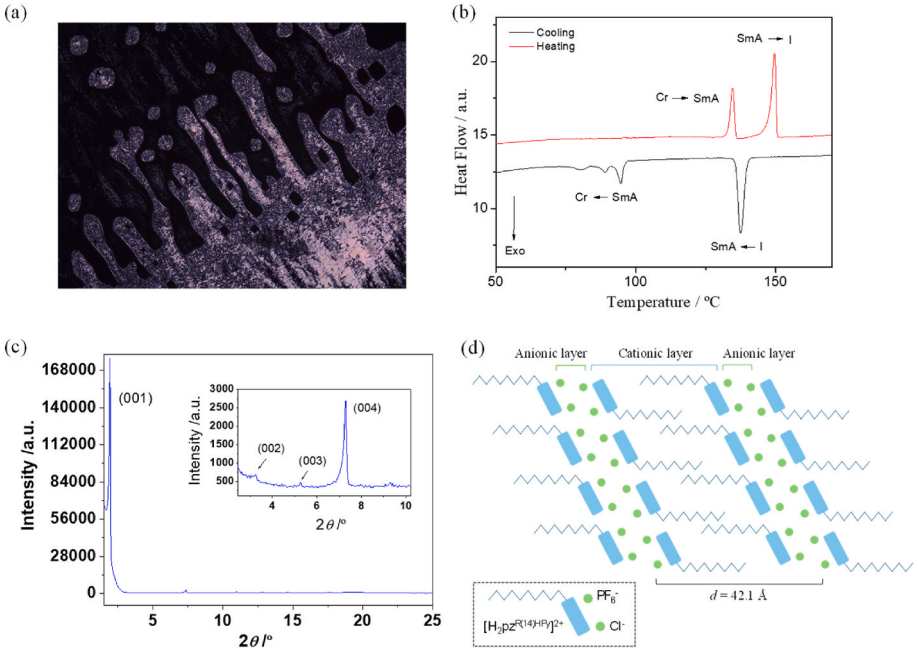

Fig. 1. Thermal study of the mesophase for the ionic salt $(H_2pz^{R(14)Hpy})Cl(PF_6)$ **4**: (a) Texture of the SmA mesophase observed by POM at 142 °C on cooling. (b) DSC trace in the first heating and cooling processes. (c) DRX diffractogram registered in the mesophase at 120 °C on cooling. (d) Schematic drawing showing the potential lamellar organization in the SmA mesophase.

Table 2
Phase behavior of the ionic salts **2**–**6**.

Numbering	Compound	Transition[a]	T/°C (ΔH/kJmol^{-1})[b]
2	$(H_2pz^{R(14)Hpy})Cl_2$	Cr - SmA	99 (56.8)
		SmA - I	200[c]
3	$(H_2pz^{R(14)Hpy})(BF_4)_2$	Cr - SmA	110 (23.6)
		SmA - I	223[c]
4	$(H_2pz^{R(14)Hpy})Cl(PF_6)$	Cr - SmA	133 (20.0)
		SmA - I	148 (42.2)
		I - SmA	142 (−43.3)
		SmA - Cr	98 (−17.1)
5	$(H_2pz^{R(14)Hpy})(OH)(SbF_6)$	Cr - Cr'	80 (9.9)
		Cr' - Cr''	122 (22.6)
		Cr - SmA	144.4 (14)
		SmA - I	295[c]
6	$[H_2pz^{R(14)Hpy}][PtCl_4]$	Cr - SmA	132 (69.7)[d]

[a] Cr, Cr', Cr'' = crystalline phases, SmA = smectic A mesophase, I = isotropic liquid.
[b] DSC onset peaks.
[c] Detected by POM. Enthalpy was not determined due to pronounced decomposition.
[d] A total decomposition occurs in the SmA mesophase at 295 °C.

cycle; however, isotropization occurs accompanied by a pronounced decomposition of samples due to the high clearing temperatures reached, which prevented the measurement of the enthalpy data. Nonetheless, the formation of batonnets that coalesce to form the typical fan-shaped texture of the SmA mesophase could be well observed for **3** on cooling (Fig. S15b). Also note that in the DSC trace of compound **4** (Fig. 1b), the solid – mesophase and the mesophase – isotrope phase transitions are clearly monitored on heating, as well as the formation of the mesophase from the isotropic liquid and the solidification process, as observed by POM.

To go further, temperature-dependent X-ray diffraction studies were made in **3** and **4** to clarify the organization of the cationic units $(H_2pz^{R(14)Hpy})^{2+}$ in the mesophase. The diffractograms registered in the SmA mesophases display a set of four reflections with a *d*-spacing ratio of 1:1/2:1/3:1/4, which confirm the lamellar nature of the mesophase (Fig. 1c and S16). The reflection associated with the molten alkyl chains is observed as a broad halo at around 4.6 Å. Indexation of reflections and structural parameters of the SmA mesophases are given in Table 3. Note that lamellar periodicity is similar for both salts regardless of the nature of the counterion. This feature points to a structural model in which cations and anions moieties form well-differentiated layers (Fig. 1d). In fact, this segregation-phase behavior may be the driving force for the formation of the mesophase in the ionic salts studied [31–33].

3.3. Photophysical study

The pyrazole-derived salts manifest luminescence properties both in solution and in the solid state, except for **6** and **7**. Photophysical characterization of all compounds in THF can be seen in Fig. 2, and data are collected in Table 4. The UV–Vis spectra show a band centered at 260 nm, and a smaller one with a maximum of 360 nm for **1** and **3**. Excitation at 260 nm gives rise to an emission band at around 360 nm in all compounds and, in the case of **3**, if excited at 360 nm, another emission band appears centered at 437 nm, suggesting the presence of an emission excimer. In all cases, luminescence quantum yields were found to be below 0.001 in solution. Regarding the solid-state emission, a great influence as a function of the counterion is observed, being absent in the case of the free ligand and the ionic salt **4**. Emission in the solid-state was easily detected after excitation at 360 nm for **2**, **3** and **5** with emission maxima at 490, 480 and 449 nm, respectively. This feature may be associated with the lesser degree of the establishment of intermolecular π···π interactions between the aromatic rings of neighboring cationic species in the order **5** < **3** < **2** [34,35].

Solid-state emission spectra were registered for **2**, **3** and **5** as a function of temperature from the solid phase to the liquid-crystalline mesophase (Fig. S17). For the three salts, the emission intensity decreases as the temperature increases, being practically quenched at the melting temperature when the mesophase is formed. Note that for **5**, a slight increase in the emission intensity occurs from 25 to 80 °C. At this temperature, a solid-solid phase transition occurs, and the fluorescence is quickly quenched as the temperature continues to increase. By cooling back to room temperature, the emission intensity is recovered only for the ionic salt **2**. In fact, it is higher than that observed initially before heating this sample. Most likely the ordering of ionic units in the mesophase is maintained after the solidification process and it improves the fluorescence properties.

As discussed previously, the dichloride salt **2** was able to manifest emission in the solid state that was not observed in the case of the pyrazole derivative. Since the presence of nitrogen atoms susceptible to be protonated, more specifically both pyridyl and pyrazole nitrogen atoms, efforts have been made to develop a system that would potentially enable the turn on effect of the solid state's emission of the pyrazole. For this purpose, supported polymer films doped with **1** have been fabricated enabling the potential opportunity to implement them as sensors and aiding on the dispersion of the compound to prevent aggregation. In line with this premise, poly(methylmethacrylate) PMMA polymer matrix has been chosen due to its well documented implementations [36–39]. The study of the sensing properties started by submerging different samples of the polymer thin film in aqueous solution of hydrochloric, sulfuric, glacial acetic, nitric, and trifluoroacetic acids for 10 min. Of all of them, only the polymer treated with HCl maintained its physical structure intact, and no visual changes were observed from its initial transparent appearance at naked eye. As expected, the doped polymer does not exhibit meaningful emission before treated. However, a substantial increase is perceived after HCl (12 M) treatment, and a band with an emission maximum at 450 nm becomes clear (Fig. 3a). Note that the differences in the solid state's emission maxima of the chloride salt **2** ($\lambda_{solution}$ = 352 nm; λ_{solid} = 490 nm) and the newly fabricated material could be attributed to the protonation of **1** in the PMMA support. Compound **1** constitutes 1 % of the material and, therefore, the ionic species are highly dispersed inside the polymer matrix, which restrict the formation of intermolecular π···π interactions between the cationic species if compared with the solid state. This fact originates a luminescence response ($\lambda_{polymer}$ = 450 nm) that is intermediate between that found for **2** in solution and in the solid state (Fig. 3b).

The elucidation about the reversibility was put forward by submerging the already treated polymer film onto an aqueous solution of NH_3 (25 % in water). Results suggest that the polymer return to its initial state, and a quenching of the emission is detected (Fig. 3a).

The reusability of the polymeric material was demonstrated by measuring the emission spectra during consecutive acid/base cycles. The turn-on and "turn-off" responses were well-detected for five cycles

Table 3
X-ray diffraction data for $(H_2pz^{R(14)Hpy})(BF_4)_2$ (**3**) at 130 °C on heating and for $(H_2pz^{R(14)Hpy})Cl(PF_6)$ (**4**) at 120 °C on cooling.

Cpd.	*d*-spacing/Å	[*hkl*][a]	Lamellar periodicity/Å[b]
3	41.6	(001)	d_{cal} = 42.6
	21.3	(002)	
	14.4	(003)	
	10.8	(004)	
	4.6[c]	–	
4	46.1	(001)	d_{cal} = 42.1
	23.8	(002)	
	12.0	(003)	
	9.7	(004)	
	4.7[c]	–	

[a] [hkl] are the Miller indices.
[b] $d_{cal} = (\Sigma l d_{00l})/N_{00l}$; where N_{00l} is the number of 00*l* reflections.
[c] Broad halo.

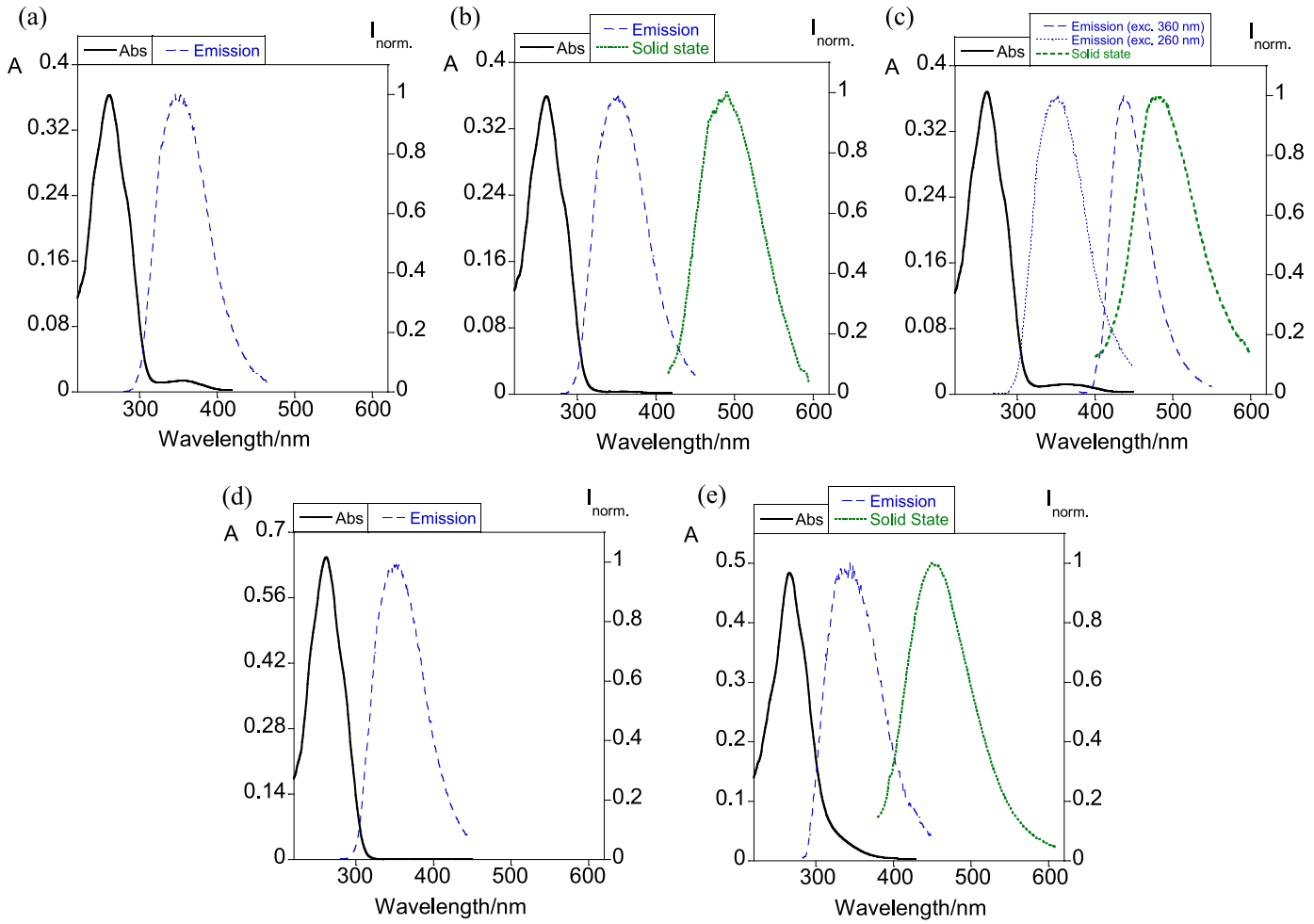

Fig. 2. Photophysical characterization for compounds (a) $Hpz^{R(14)py}$ (**1**), (b) $(H_2pz^{R(14)Hpy})Cl_2$ (**2**), (c) $(H_2pz^{R(14)Hpy})(BF_4)_2$ (**3**), (d) $(H_2pz^{R(14)Hpy})Cl(PF_6)$ (**4**) and (e) $(H_2pz^{R(14)Hpy})(OH)(SbF_6)$ (**5**). [ ] = 1.0×10^{-5} M; slit width for both excitation and emission in solution and/or solid state: 3 nm (2 nm for **3** and **5** in the solid state).

Table 4
Photophysical data.

Cpd.	λ_{abs}/ nm	λ_{em} [nm]	$\varepsilon/10^4$ cm^{-1} M^{-1}	Stokes shift/cm^{-1}	λ_{em}^{Solid}/ nm[a]
1	261, 355	353 (261)	3.86 (261), 0.16 (355)	9986 (261)	–
2	261	352	3.60	9905	490
3	261, 362	353 (261), 437 (362)	3.81 (261), 0.13 (362)	9986 (261), 4741 (362)	479
4	262	349	6.39	9515	–
5	266	337	5.01	7920	449

[a] The emission spectra were registered under excitation at 360 nm at room temperature.

after the exposure of the sample to HCl and subsequent treatment with ammonia (Fig. 3c and d). Although the intensity of the emission band at 450 nm slightly decreases after each cycle, the enhanced luminescence is still clearly detectable under UV light. Thus, it presents the fundamental characteristic to be implemented several times as an economic and sustainable sensor of acidic environments giving value to its applicability.

Further experiments were performed by submerging the PMMA material in HCl solutions at different concentrations ranging from 6 to 10 M. As expected, the 10-min mark implemented for the remaining studies increasingly prevents the polymer to reach the emission that is held when submerged at 12 M, demonstrating that the concentration of protons in these solutions is not sufficient to enable the complete protonation of the pyridyl and pyrazole nitrogen atoms (Fig. 4a). This feature makes the new polymer capable to detect selectively the presence of HCl in aqueous solutions as a function of the emission intensity, which shows a linear dependence on HCl concentration (Fig. 4b).

UV–Vis absorption spectra were also measured and plotted as a function of the HCl concentration, as shown in Fig. S18. Although a slight bathochromic shift occurs when the polymer is treated with HCl, no clear dependence with HCl concentration is observed. This could be due to a lack of homogeneity in the thickness of the polymers as a result of the physical changes that they undergo after HCl treatment.

3.4. Theoretical study

Density functional theory (DFT) calculation was performed to understand the origin of the fluorescent turn-on response of the pyrazole derivative when protonation to occurs. The ground state (GS) structures of both the neutral and protonated forms were optimized using the CAM-B3LYP functional with 6-31+G(2d,p) basis set, replacing the aliphatic chain by a methyl group in order to reduce the calculation cost. Bond lengths and angles are collected in Tables S1–S8, and Fig. 5a and b and S19a,b display the optimized GS structures of **1** and **1-2H**$^+$ in the gas phase and in THF solvent. As observed, the overall structure of **1** shows a high planarity, although the pyridine and benzene rings are slightly rotated with respect to the pyrazole plane. In the gas phase, the torsion angles are −166.7 Å (N1–C5–C6–C7), −166.3 Å (C4–C5–C6–C10),

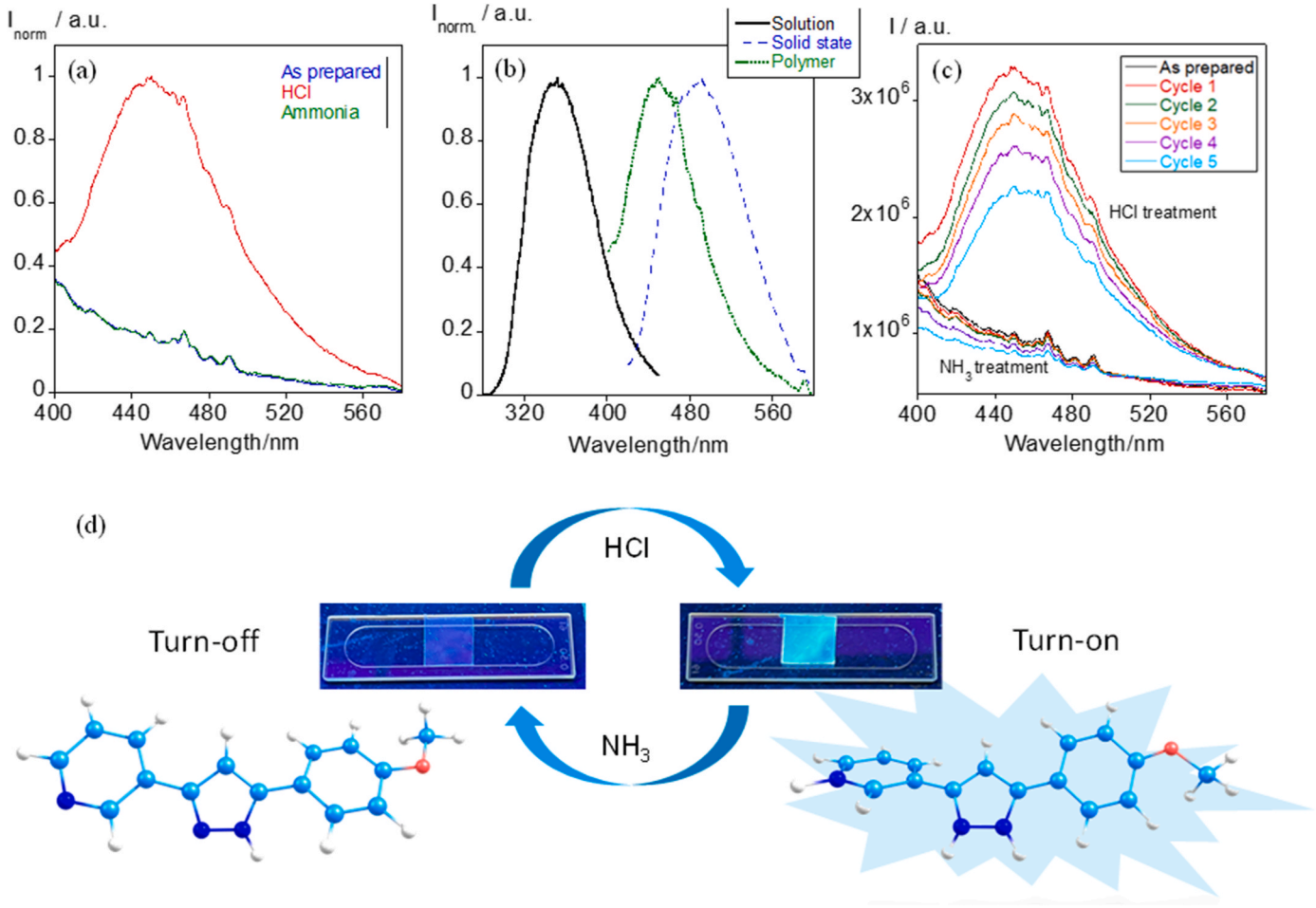

Fig. 3. Sensing properties of the PMMA film doped with $Hpz^{R(14)py}$ **1**. (a) Normalized emission spectra recorded prior and after treatment with HCl (12 M), and sequent immersion in a NH_3 solution. (b) Emission spectra in solution, solid state and inside the PMMA polymer matrix. (c) Emission spectra registered after HCl and ammonia treatments during consecutive acid/base cycles. (d) Images showing the turn-on response of the PMMA sensor under UV light (λ_{exc} = 365 nm). Slit width: 2.5 nm.

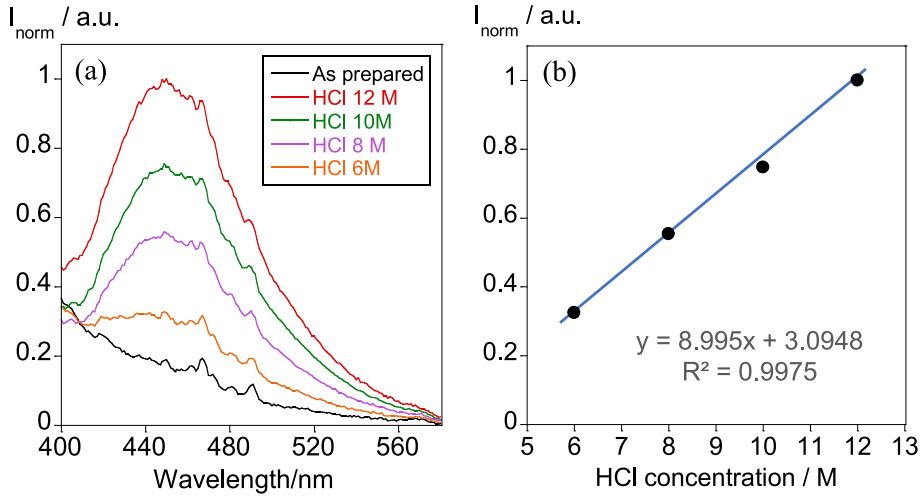

Fig. 4. (a) Emission spectra recorded after exposure at different concentrations of HCl aqueous solutions (slit width: 2.5 nm). (b) Linearity curve showing the dependence between the luminescence emission intensity and the HCl concentration.

146.7 Å (N2–C3–C11–C16) and 146.0 Å (C4–C3–C11–C12). When calculated in THF, these angles slightly adjust to −163.3, −162.9, 150.6 and 147.0 Å, respectively. The C–C and C–N bond distances of the three rings show values that are consistent with a delocalized π-system, as expected. In contrast, the protonated species **1-2H**$^+$ exhibits more pronounced rotation of the pyridine ring with respect to the pyrazole plane. The torsion angles in the gas phase are −138.7 Å (N1–C5–C6–C7), −135.3 Å (C4–C5–C6–C10), −168.0 Å (N2–C3–C11–C16) and −169.0 Å

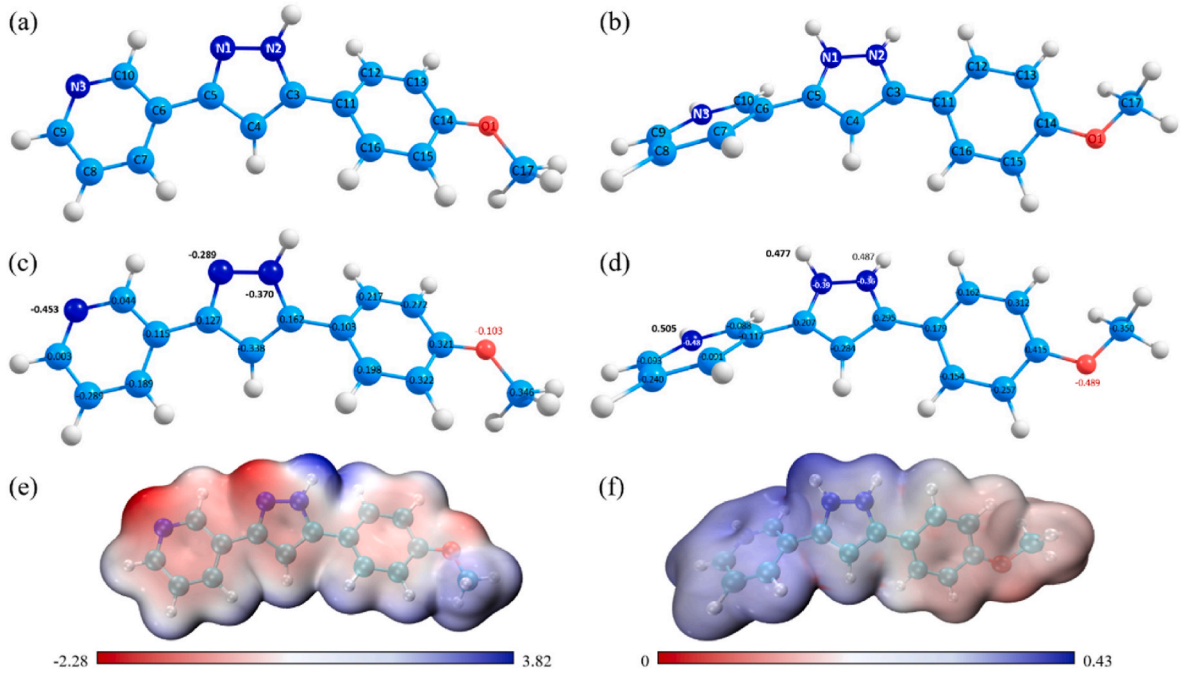

Fig. 5. DFT calculations performed for **1** and **1-2H**$^+$ species at the CAM-B3LYP/6–31+G(2d,p) level in the gas phase: (a,b) Optimized structures showing the numbering used. (c,d) Natural bond orbital atomic charges. (e,f) Molecular electrostatic potential surface maps.

(C4–C3–C11–C12). In THF, these angles shift to −138.5, −137.7, −154.2 and −153.9 Å, respectively. The presence of the THF solvent slightly moderates these torsion angles, suggesting solvent effects that stabilize certain conformations.

Fig. 5c,d and S19c,d display the natural bond orbital (NBO) atomic charges for the structure of **1** and **1-2H**$^+$, calculated in the gas phase and in THF. For compound **1**, the pyrazole nitrogen atoms (N1 and N2) carry negative charges of −0.289 and −0.370 e in the gas phase, and −0.314 and −0.369 e in THF, respectively. The nitrogen atom of the pyridine moiety (N3) presents the highest degree of negative charge with a value of −0.453 e in the gas phase and −0.482 e in THF. Consistent with it, adjacent carbon atoms are positively charged whereas those furthest from the nitrogen atoms have negative charge values ranging between −0.115 and −0.338 e (in the gas phase) and −0.094 e and −0.344 e (in THF). This evidences that the negative charge is delocalized on the aromatic rings, as also happens in the benzene group, and explains the existence of intermolecular π···π interactions in the solid state. Similar features are observed for **1-2H**$^+$ but note that the new protons bonded to N3 and N1 atoms exhibit a high positive charge (0.505 and 0.477 e in the gas phase; 0.513 e and 0.484 e in THF) that counteracts the negative charges of the nitrogen atoms.

Visualization of the charge density can be seen in the molecular electrostatic potential (MEP) surface maps depicted in Fig. 5e,f and S19e,f. Results are in good agreement with the NBO atomic charges, showing for **1** an area of high negative charge density mainly located over the N3 and N1 atoms. Likewise, the electron delocalization of the aromatic rings is also detected. However, the presence of THF results in an increased positive charge density, which can be ascribed to solvent-induced polarization effects (Fig. S19e). It has been established that, when employed as a polar solvent, THF stabilizes certain partial charges and redistributes the electron density. Conversely, the MEP surface map for **1-2H**$^+$ exhibits a generalized positive charge density throughout the structure, attributable to protonation, especially around the pyridinium and pyrazolium fragments. The addition of THF has been shown to results in an increase in negative charge regions, suggesting that the solvent stabilizes the positive charges to a certain extent, thereby promoting a more balanced charge distribution around the pyridinium and pyrazolium fragments in solution compared to the gas phase (Fig. S19f).

Frontier molecular orbitals have also been analyzed by DFT to gain insight into the electronic distribution and photophysical of compounds **1** and **1-2H**$^+$. As shown in Fig. 6 and S20, the HOMO and LUMO ones in **1** appear delocalized on the whole molecule, which supports the fact of the existence of charge transfers between any of the three aromatic rings. This delocalization suggests the occurrence of intramolecular charge transfer (ICT) across the molecule. Instead, both the HOMO and the LUMO are clearly localized in the structure of **1-2H**$^+$, the first one over the pyrazole and benzene moieties, and the second one extended around the pyrazole and pyridine groups. The HOMO-LUMO energy gap was calculated to be 6.47 and 4.55 eV for **1** and **1-2H**$^+$, respectively, in the gas phase. When solvent effects (THF) are included, the energy gap slightly decreases to 6.43 eV for **1,** and increased to 5.81 eV for **1-2H**$^+$. The energy decrease observed in **1-2H**$^+$ is associated with a stabilization of the frontier orbitals, especially for the LUMO, which would explain the appearance of the new emission band at low energies in the protonated species and, concomitantly, support the fluorescence turn-on response found in **1** after treatment with acids. The HOMO-1, HOMO-2, LUMO+1 and LUMO+2 for **1** and **1-2H**$^+$ were also calculated in both the gas phase and THF solvent (Figs. S21–S24).

In order to provide further support for the photophysical study, time-dependent density functional theory (TD-DFT) calculations were carried out with the aim of characterizing the excited states (Tables S9–S12). For **1**, the lowest singlet excited state (S_1) corresponds to a HOMO → LUMO transition, with calculated emission wavelengths of 303 nm in the gas phase and 323 nm in THF. These results are in reasonable agreement with the band emission observed in solution at 353 nm (see Table 4). In the case of **1-2H**$^+$, the lowest-energy transition in the gas phase is not permitted, and the dominant radiative decay corresponds to the third singlet excited state (S_3), characterized mainly by a HOMO-1 → LUMO+1 excitation, emitting at 441 nm. However, in THF, the emissive state is the S_1, primarily $S_0 \rightarrow S_1$, with a computed emission value of 409 nm, closer to the experimental value of around 350 nm in solution for those compounds containing the cationic fragment, i.e. for **2**–**5**. While **1** is non-emissive in the solid state, compounds **2**–**5** show solid-state emission bands centered between 490 and 449 nm as a function of the counterions present in the structure (Table 4), which is consistent with

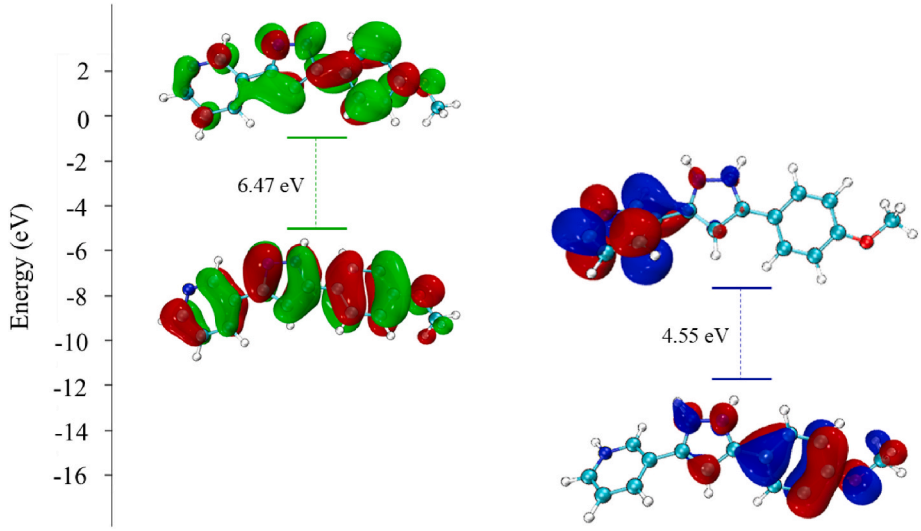

Fig. 6. DFT plot showing the electronic distribution of the HOMO and LUMO for the pyrazole derivative in its neutral (**1**) and ionic (**1-2H**$^{+}$) forms in the gas phase. The HOMO-LUMO energy GAP is also indicated.

the theoretical value found in the gas phase (441 nm) and supports the turn-on behavior observed under protonation of **1** with HCl in the solid state or in the PMMA matrix.

4. Conclusions

A new series of ionic salts derived from a pyridylpyrazolium cation $(H_2pz^{R(14)Hpy})^{2+}$ has been prepared. The salts have been obtained by anion exchange from the dichloride precursor derivative $(H_2pz^{R(14)Hpy})Cl_2$, which was in turn obtained from the neutral pyrazole compound by treatment with HCl. The investigation shows that the nature of the counterion is crucial for the composition and properties of the new species. In particular, those salts with PF_6^- and SbF_6^- anions lead to the formulation $(H_2pz^{R(14)Hpy})Cl(PF_6)$ and $(H_2pz^{R(14)Hpy})(OH)(SbF_6)$, while the remaining compounds involve the total substitution of the two Cl^- ions of the precursor, leading to salts of the type $(H_2pz^{R(14)Hpy})A_n$ (n = 2, $A = BF_4^-$; n = 1, A = $[PdCl_4]^{2-}$, $[PtCl_4]^{2-}$). The new species, except for the derivative bearing $[PdCl_4]^{2-}$ as counterion, exhibit mesomorphism and form smectic A mesophases during both the heating and cooling cycles. Additionally, they also show luminescence properties in solution and in the solid state. In particular, the pyrazole precursor $Hpz^{R(14)py}$ has been used as a dopant for the fabrication of polymeric materials. The photophysical characterization of this material reveals the absence of luminescent emission, as expected, but under HCl treatment an intense blue light is originated. This acidochromic behavior has been attributed to the reversible protonation of the nitrogen atoms of the pyrazole and pyridine groups. Interestingly, it can be reversed by submerging the polymer in an ammonia solution, allowing the polymer to be recovered and used again as a reliable, economic and sustainable sensor of acidic aqueous environments.

CRediT authorship contribution statement

Rosario Criado: Writing – review & editing, Methodology, Investigation, Data curation. **Frederico Duarte:** Writing – review & editing, Investigation, Data curation. **Irene Caro-Campos:** Visualization, Investigation, Data curation. **Mercedes Cano:** Writing – review & editing, Conceptualization. **Santiago Herrero:** Writing – review & editing, Methodology, Funding acquisition. **Carlos Lodeiro:** Writing – review & editing, Supervision, Project administration, Funding acquisition. **Cristián Cuerva:** Writing – review & editing, Writing – original draft, Supervision, Methodology, Investigation.

Funding sources

This work received support from PT national funds (FCT/MCTES, Fundação para a Ciência e Tecnologia and Ministério da Ciência, Tecnologia e Ensino Superior) through the projects UIDB/50006/2020 and UIDP/50006/2020. This work received support from PROTEOMASS Scientific Society through the General Funding Grant 2023–2024, and the projects #PM001/2019 and #PM003/2016. The authors also gratefully acknowledge financial support from the Complutense University of Madrid, project PR3/23–30828 and to the Community of Madrid, project TEC-2024/TEC-85.

Declaration of competing interest

The authors declare that they have no known competing financial interests or personal relationships that could have appeared to influence the work reported in this paper.

Acknowledgments

R. C. thanks to Rodrigo González for his help in the measurements of the solid-state UV-Vis absorption spectra. I.C.C wish to thank Felix León from the IIQ for the discussions that helped her focus the development of the calculations presented in this work. F.D. thanks to FCT/MCTES (Portugal) for his doctoral grant 2021.05161.BD. C.L thanks the RSC by the financial support through the GREEN Lab sustainable laboratories grant for Reducing the Water misuse in a Nano@Dyes Synthesis Lab 2024 – ID L23-8861107285.

Appendix A. Supplementary data

Supplementary data to this article can be found online at https://doi.org/10.1016/j.dyepig.2025.113050.

Data availability

Data will be made available on request.

References

[1] Cuerva C, Cano M, Lodeiro C. Advanced functional luminescent metallomesogens: the key role of the metal center. Chem Rev 2021;121:12966–3010.
[2] Martínez-Ceberio C, Carmen Torralba M, Duarte F, Herrero S, Cano M, Lodeiro C, Cuerva C. Mesomorphism and luminescence in coordination compounds and ionic

salts based on pyridine-functionalized β-diketones. Influence of the pyridine nitrogen position. J Mol Liq 2023;385:122290.
[3] Cuerva C, Cano M, Schmidt R. Improving the mesomorphism in bispyrazolate Pd (II) metallomesogens: an efficient platform for ionic conduction. Dalton Trans 2023;52:4684–91.
[4] Cuerva C, Fernández-Lodeiro J, Cano M, Capelo-Martínez JL, Lodeiro C. Water-soluble hollow nanocrystals from self-assembly of AIEE-active Pt(II) metallomesogens. Nano Res 2021;14:245–54.
[5] Ovejero P, Asensio E, Heras JV, Campo JA, Cano M, Torres MR, Núñez C, Lodeiro C. Silver–pyrazole complexes as hybrid multifunctional materials with metallomesogenic and photoluminescent behaviour. Dalton Trans 2013;42:2107–20. https://pubs.rsc.org/en/content/articlelanding/2013/dt/c2dt31750h.
[6] Cuerva C, Campo JA, Cano M, Lodeiro C. Multi-stimuli-responsive properties of aggregation-enhanced emission-active unsymmetrical PtII metallomesogens through self-assembly. Chem Eur J 2019;25:12046–51.
[7] Cîrcu V. Ionic liquid crystals based on pyridinium salts. In: Handy S, editor. Ionic liquids - progress and developments in. Rijeka: IntechOpen; 2017. https://www.intechopen.com/chapters/52994.
[8] Xiao Q, Duan Y, Chen Y, Liu D, Xiong W, Cheng X. Synthesis, self-assembly, photoreactivity and application of an α-cyanostilbene pyridinium luminescent ionic liquid crystal. J Mol Struct 2025;1338:142327.
[9] Wang R-T, Jane Tsai S-J, Lee G-H, Lai CK. Aggregation−induced emissions in columnar wedge−shaped pyridinium−based ionic liquid crystals. Dyes Pigments 2020;173:107913.
[10] Bhowmik PK, Chen SL, King D, Han H, Bolyard Z, Schmiedl C, et al. Dicationic ionic liquid crystals: synthesis, characterization, optical properties, and ionic conductivity of bis(4-oligoethyleneoxyphenyl) viologen bistosylate salts. J Mol Liq 2024;398:124140.
[11] Filippi NG, Mezalira DZ, Ovalle S, Westphal E. Study of the mesomorphic behaviour through the structure modification of azo and acetylene pyridinium and imidazolium-based ionic liquid crystals. Liq Cryst 2016;43:2163–90.
[12] Salikolimi K, Sudhakar AA, Ishida Y. Functional ionic liquid crystals. Langmuir 2020;36:11702–31.
[13] Sudholter EJR, Engberts JBFN, De Jeu WH. Thermotropic liquid-crystalline behavior of some single- and double-chained pyridinium amphiphiles. J Phys Chem 1982;86:1908–13.
[14] Pastor MJ, Cuerva C, Campo JA, Schmidt R, Torres MR, Cano M. Diketonylpyridinium cations as a support of new ionic liquid crystals and ion-conductive materials: analysis of counter-ion effects. Materials 2016;9:360.
[15] Jiménez R, Duarte F, Nuti S, Campo JA, Lodeiro C, Cano M, Cuerva C. Thermochromic and acidochromic properties of polymer films doped with pyridyl-β-diketonate boron(III) complexes. Dyes Pigments 2020;177:108272.
[16] Ruan Q, Yao M, Yuan D, Dong H, Liu J, Yuan X, et al. Ionic liquid crystal electrolytes: fundamental, applications and prospects. Nano Energy 2023;106:108087.
[17] Bendaoud U, Bhowmik PK, Chen SL, Han H, Cox SL, Liebsch J, et al. Modulating the conductivity of light-responsive ionic liquid crystals. Molecules 2024;29:4459.
[18] Molahalli V, Hirankittiwong P, Sharma A, Laeim H, Shetty A, Chattham N, et al. Roadmap on ionic liquid crystal electrolytes for energy storage devices. Mater Sci Eng B 2024;305:117369.
[19] Gaussian 16, Revision C. 01, Frisch, M.J.; Trucks, G.W.; Schlegel, H.B.; Scuseria, G. E.; Robb, M.A.; Cheeseman, J.R.; Scalmani, G.; Barone, V.; Petersson, G.A.; Nakatsuji, H.; Li, X.; Caricato, M.; Marenich, A.V.; Bloino, J.; Janesko, B.G.; Gomperts, R.; Mennucci, B.; Hratchian, H.P.; Ortiz, J.V.; Izmaylov, A.F.; Sonnenberg, J.L.; Williams-Young, D.; Ding, F.; Lipparini, F.; Egidi, F.; Goings, J.; Peng, B.; Petrone, A.; Henderson, T.; Ranasinghe, D.; Zakrzewski, V.G.; Gao, J.; Rega, N.; Zheng, G.; Liang, W.; Hada, M.; Ehara, M.; Toyota, K.; Fukuda, R.; Hasegawa, J.; Ishida, M.; Nakajima, T.; Honda, Y.; Kitao, O.; Nakai, H.; Vreven, T.; Throssell, K.; Montgomery, J.A., Jr.; Peralta, J.E.; Ogliaro, F.; Bearpark, M.J.; Heyd, J.J.; Brothers, E.N.; Kudin, K.N.; Staroverov, V.N.; Keith, T.A.; Kobayashi, R.; Normand, J.; Raghavachari, K.; Rendell, A.P.; Burant, J.C.; Iyengar, S.S.; Tomasi, J.; Cossi, M.; Millam, J.M.; Klene, M.; Adamo, C.; Cammi, R.; Ochterski, J.W.; Martin, R.L.; Morokuma, K.; Farkas, O.; Foresman, J.B.; Fox, D.J. Gaussian, Inc., Wallingford CT, 2016.
[20] Yanai T, Tew DP, Handy NC. A new hybrid exchange-correlation functional using the Coulomb-attenuating method (CAM-B3LYP). Chem Phys Lett 2004;393:51–7.
[21] Jacquemin D, Perpète EA, Medved M, Scalmani G, Frisch MJ, Kobayashi R, Adamo C. First hyperpolarizability of polymethineimine with long-range corrected functionals. J Chem Phys 2007;126:191108. https://pubs.aip.org/aip/jcp/article/126/19/191108/929387/First-hyperpolarizability-of-polymethineimine-with.
[22] Petersson GA, Bennett A, Tensfeldt TG, Al-Laham MA, Shirley WA. Mantzaris. A complete basis set model chemistry. I. The total energies of closed-shell atoms and hydrides of the first-row elements. J Chem Phys 1988;89:2193–218.
[23] Marenich AV, Cramer CJ, Truhlar DG. Universal solvation model based on solute electron density and on a continuum model of the solvent defined by the bulk dielectric constant and atomic surface tensions. J Chem Phys B 2009;113:6378–96.
[24] Zhurko G.A., Zhurdko D.A. Chemcraft - graphical software for visualization of quantum chemistry computations. Version 1.8, build 682. https://www.chemcraftprog.com.
[25] VMD User's Guide. Theoretical and computational biophysics group. University of Illinois at Urbana-Champaign; 2016. Available at:, Version 1.9.3. http://www.ks.uiuc.edu/Research/vmd/.
[26] Charaf-Eddin A, Planchat A, Mennucci B, Adamo C, Jacquemin D. Choosing a functional for computing absorption and fluorescence band shapes with TD-DFT. J Chem Theor Comput 2013;9:2749–60.
[27] Fleming I, Williams D. Infrared and raman spectra. In: Fleming I, Williams D, editors. Spectroscopic methods in organic chemistry. Cham: Springer International Publishing; 2019. p. 85–121. https://link.springer.com/book/10.1007/978-3-030-18252-6.
[28] Pastor MJ, Sánchez I, Campo JA, Schmidt R, Cano M. New pyrazolium salts as a support for ionic liquid crystals and ionic conductors. Materials 2018;11:548.
[29] Bhat SV, Swamynathan K, Kumar S. Synthesis and mesomorphic characterization of novel liquid crystals derived from bioactive natural sterols. J Mol Liq 2021;326:115216.
[30] Mayoral MJ, Ovejero P, Campo JA, Heras JV, Pinilla E, Torres MR, et al. Silver and gold luminescent metallomesogens based on pyrazole ligands. Dalton Trans 2008:6912–24.
[31] Kato T. Self-assembly of phase-segregated liquid crystal structures. Science 2002;295:2414–8.
[32] Ichikawa T, Sasaki Y, Kobayashi T, Oshiro H, Ono A, Ohno H. Design of ionic liquid crystals forming normal-type bicontinuous cubic phases with a 3D continuous ion conductive pathway. Crystals 2019;9:309.
[33] Hamaguchi K, Ichikawa R, Kajiyama S, Torii S, Hayashi Y, Kumaki J, et al. Gemini thermotropic smectic liquid crystals for two-dimensional nanostructured water-treatment membranes. ACS Appl Mater Interfaces 2021;13:20598–605.
[34] Wang W-J, Hao L, Chen C-Y, Qiu Q-M, Wang K, Song J-B, et al. Red-shift in fluorescence emission of D–A type asymmetrical Zn(II) complexes by extending the π–π stacking interaction. RSC Adv 2017;7:20488–93. https://pubs.rsc.org/en/content/articlelanding/2017/ra/c7ra01135k.
[35] Cui Y, Liu Q-D, Bai D-R, Jia W-L, Tao Y, Wang S. Organoboron compounds with an 8-hydroxyquinolato chelate and its derivatives: substituent effects on structures and luminescence. Inorg Chem 2005;44:601–9.
[36] Hassanien AM, Alanazi HTA, Almutairi FN, Alotaibi A, AlZaidy GA, Kamal AM, et al. Tuning the optical properties of PMMA polymer by using subphthalocyanine dye and metal oxide nanoparticles for flexible optoelectronic devices. Opt Quant Electron 2024;56:1431. https://link.springer.com/article/10.1007/s11082-024-07311-9.
[37] Qian C, Ma Z, Fu X, Zhang X, Li Z, Jin H, et al. More than carbazole derivatives activate room temperature ultralong organic phosphorescence of benzoindole derivatives. Adv Mater 2022;34:2200544. https://advanced.onlinelibrary.wiley.com/doi/10.1002/adma.202200544.
[38] Li S-Y, Zong Y, Liu B-H, Liu N, Wu Z-Q. Helix-induced full-color circularly polarized luminescence films with multiple information encryption and multi-stimuli responsiveness. Chem Sci 2025;16:5036–42.
[39] Mara D, Kaczmarek AM, Artizzu F, Abalymov A, Skirtach AG, Van Hecke K, et al. Luminescent PMMA films and PMMA@SiO_2 nanoparticles with embedded Ln^{3+} complexes for highly sensitive optical thermometers in the physiological temperature range. Chem Eur J 2021;27:6479–88.